

Deep learning reconstruction of digital breast tomosynthesis images for accurate breast density and patient-specific radiation dose estimation

Jonas Teuwen^{a,b,1}, Nikita Moriakov^{a,b,1}, Christian Fedon^a, Marco Caballo^a, Ingrid Reiser^e, Pedrag Bakic^{f,g}, Eloy García^c, Oliver Diaz^d, Koen Michielsen^a, Ioannis Sechopoulos^{a,h}

^aDepartment of Medical Imaging, Radboud University Medical Center, the Netherlands

^bDepartment of Radiation Oncology, Netherlands Cancer Institute, the Netherlands

^cVall d'Hebron Institute of Oncology, VHIO, Spain

^dDepartment of Mathematics and Computer Science, University of Barcelona, Spain

^eDepartment of Radiology, The University of Chicago, USA

^fDepartment of Radiology, University of Pennsylvania, USA

^gDepartment of Translational Medicine, Lund University, Sweden

^hDutch Expert Centre for Screening (LRCB), the Netherlands

Abstract

The two-dimensional nature of mammography makes estimation of the overall breast density challenging, and estimation of the true patient-specific radiation dose impossible. Digital breast tomosynthesis (DBT), a pseudo-3D technique, is now commonly used in breast cancer screening and diagnostics. Still, the severely limited 3rd dimension information in DBT has not been used, until now, to estimate the true breast density or the patient-specific dose. In this study, we propose a reconstruction algorithm for DBT based on deep learning specifically optimized for these tasks. The algorithm, which we name DBToR, is based on unrolling a proximal primal-dual optimization method, where the proximal operators are replaced with convolutional neural networks and prior knowledge is included in the model. This extends previous work on a deep learning based reconstruction model by providing both the primal and the dual blocks with breast thickness information, which is available in DBT. Training and testing of the model were performed using virtual patient phantoms from two different sources. Reconstruction performance, as well as accuracy in estimation of breast density and radiation dose, was estimated, showing high accuracy (density $< \pm 3\%$; dose $< \pm 20\%$), without bias, significantly improving on the current state-of-the-art. This work also lays the groundwork for developing a deep learning-based reconstruction algorithm for the task of image interpretation by radiologists.

Keywords: digital breast tomosynthesis, reconstruction, deep learning

1. Introduction

Breast cancer screening with mammography has proven effective in reducing breast cancer related mortality (Plevritis et al., 2018). However, since mammography

is a 2D imaging modality, it results in the projection of the internal tissue of the breast onto a single plane, yielding tissue superposition. This results in a lower sensitivity and specificity, especially with dense breasts. In addition, this lack of information on the true tissue distribution in the vertical (x-ray source to detector) direction limits the ability to accurately estimate the breast density (i.e., the proportion of the breast that consists of fibroglandular tissue). Up to now, estimates of breast density from mammography necessitated the use of models of the image acquisi-

*Corresponding author: Ioannis Sechopoulos

Email address: ioannis.sechopoulos@radboudumc.nl

(Ioannis Sechopoulos)

¹Equal contribution.

tion process and assumptions and simplifications regarding tissue distribution. Although these models have been characterized for consistency and precision, their accuracy is unknown. Estimation of breast density is of intense interest due to it being an important factor for both masking effects and breast cancer risk (McCormack, 2006). As a result of its significance, breast density reporting is now mandated by law in several states in the USA. This makes it especially important that we use methods that provide reliable, robust, and consistent breast density estimates.

In addition to limiting the accuracy of breast density estimation, the 2D nature of mammography makes it impossible to estimate the radiation dose received by a specific patient during image acquisition. This is because, in breast imaging, the dose of interest is only that to the fibroglandular tissue, since this is the tissue at risk of developing breast cancer (Dance and Sechopoulos, 2016), and to determine this dose it is necessary to know its vertical location within the breast. Therefore, currently all breast dosimetry is based on dose estimates using a model breast, which does not reflect the dose deposited in the actual patient breast. It has been shown that the use of a model breast results in an average over-estimation of the true patient breast of 30% and that this error can be as high as 120%, if not more (Dance et al., 2005; Sechopoulos et al., 2012; Hernandez et al., 2015). Even if a more accurate, unbiased model of the average breast is developed, an effort which is currently ongoing (Arana Peña et al., 2020), the over 100% error in patient-specific dose estimates by use of a population-wide model will not be ameliorated. To obtain accurate radiation dose estimates, the actual amount and position of the fibroglandular tissue in the actual patient’s breast needs to be considered. In this work we address both the estimation of amount and location of the fibroglandular tissue within each patient’s breast, resulting in accurate estimates of both the breast density and fibroglandular dose.

Digital breast tomosynthesis (DBT) has been introduced over the last two decades to decrease the impact of tissue superposition in mammography, by providing limited depth information, resulting in improved detection and diagnosis performance (Zackrisson et al., 2018; Zuley et al., 2013). Hence, DBT is rapidly replacing digital mammography as the primary x-ray technique for breast imaging (Niklason et al., 1997). DBT imaging consists of acquiring several low-dose planar x-ray projections over

a limited angle. These projections are then used to reconstruct a pseudo-3D volume, albeit with very limited vertical spatial resolution. Even so, the introduction of an imaging modality that provides some vertical information into widespread use for screening provides the opportunity, for the first time, to obtain accurate estimates of the breast density and fibroglandular dose. However, given the very poor spatial resolution in the vertical direction obtained with all current DBT reconstruction algorithms, the localization of the fibroglandular tissue in DBT images has proven extremely challenging. Previous efforts to achieve this have not resulted in improvements over the model-based dose estimates obtained from 2D imaging (Geeraert, 2014), or have involved algorithms that require a lot of manual input, making them challenging to implement clinically (Förnvik et al., 2018).

In general, reconstruction of a 3D volume from computed tomography (CT) or DBT projections is an inverse problem, and there exist multiple algorithms for solving such problems. For DBT, in particular, the choice of the reconstruction algorithm and regularization parameters can greatly influence the reconstruction quality, as was shown in previous work (Rodriguez-Ruiz et al., 2017; Michielsen et al., 2016). In this work, we propose a new approach to DBT reconstruction, based on our earlier work (Moriakov et al., 2019), using deep learning methods, that results in the 3D representation of the imaged breast optimized for estimation of the true distribution of the fibroglandular tissue. This in turn allows for accurate estimation of both the breast density and the radiation dose imparted on it, improving significantly upon the state-of-the-art.

A recent and very promising development in medical imaging reconstruction is using methods that rely on deep learning (Arridge et al., 2019). The goal of this paper is to show the potential of such methods for the problem of DBT reconstruction, using the quantitative estimation of breast density and radiation dose as the target application. For this, we extended our previous results on DBT reconstruction (Moriakov et al., 2019) and investigate a data-driven reconstruction algorithm called Deep Breast Tomographic Reconstruction (DBToR), where the reconstruction is computed from projection data with a deep neural network. To train the model, and to test the performance of DBToR for the tasks of breast density and radiation dose estimation, we used dedicated breast CT

images, where the tissue distribution is known, and use a finite-element model to simulate the change in the tissue distribution when under compression in DBT. In addition to these images, we also evaluate the model on simulated breast phantoms.

1.1. Our contribution

In this work, we show: (i) the feasibility of reconstruction of DBT using deep learning, having developed a novel deep learning-based architecture to reconstruct DBT; (ii) that the resulting reconstructions have greatly improved vertical resolution compared to state-of-the-art analytical and iterative reconstruction methods; (iii) that the proposed reconstruction method is able to provide accurate breast density estimates; and (iv) that the dense tissue location information results in accurate patient-specific dosimetric estimates.

2. Deep learning-based reconstruction

Before we describe our model in more detail, we give a brief overview of reconstruction problems formulated as inverse problems.

2.1. Inverse problems and DBT reconstruction

Image reconstruction can be stated as an inverse problem. Formally this means that given an image $x \in X$ and measured projection data $y \in Y$, we have

$$y = Ax + \eta \quad (1)$$

where $A : X \rightarrow Y$ is the forward operator, or projection operator, that models how the image x gives rise to the projection Ax in the absence of noise, and η is a Y -valued random variable modeling the noise component of the measurements. Typically, the spaces X and Y are Banach spaces, and here X and Y denote the spaces of functions describing true breast anatomy and measurements, respectively. The noise vector η can typically be considered to be Gaussian when the photon count is large enough, as is typically the case in transmission imaging.

This problem can also be considered from a Bayesian perspective, where X and Y are probability spaces and the

probability distribution $x \sim P(x)$ on X is called the *prior*. Bayes theorem states that

$$P(x|y) = \frac{P(y|x)P(x)}{P(y)}, \quad (2)$$

where the conditional probability $P(y|x)$ is called the *likelihood* of data y , which expresses the probability of taking measurements y from given data x . The likelihood is derived from the forward model, using the knowledge of the forward operator A and the noise distribution η .

The goal of reconstruction is to retrieve the image x from the noise-corrupted measurements y . Inversion of the operator A is generally an ill-posed problem, and there exist different approaches towards estimating x . From a probabilistic perspective, two of the most important estimators are *Maximum Likelihood* and *Bayes* estimators. In the *Maximum Likelihood* estimator, the estimated x is given by finding x_{ML} that maximizes the likelihood of data y . For Bayes estimator, the goal is minimizing the expected loss over all estimators $\hat{x} : Y \rightarrow X$ that give an estimate of x given measurements y . That is,

$$\hat{x}_{\text{Bayes}} := \underset{\hat{x}: Y \rightarrow X}{\operatorname{argmin}} \mathbf{E}_{x \sim X} (\hat{x}(y) - x)^2. \quad (3)$$

It can be shown that the Bayes estimate of the unknown parameter \hat{x}_{Bayes} from measurements y is simply the mean of the posterior distribution $P(x|y)$, that is,

$$\hat{x}_{\text{Bayes}}(y) = \int_X x P(x|y) dx. \quad (4)$$

In our approach, we will obtain a neural network approximation to the Bayes estimator \hat{x}_{Bayes} , where argmin in Equation (3) is taken over the estimators given by a family of neural networks and where optimization is performed using minibatch stochastic gradient optimization.

2.2. DBT neural network

The DBToR algorithm, a data-driven algorithm designed for DBT reconstruction, extends the Learned Primal-Dual (LPD) reconstruction algorithm (Adler and Öktem, 2018) to incorporate additional prior information about the geometry in the form of the thickness measurement of the breast under compression in DBT (as measured by the DBT device and stored in the DICOM image

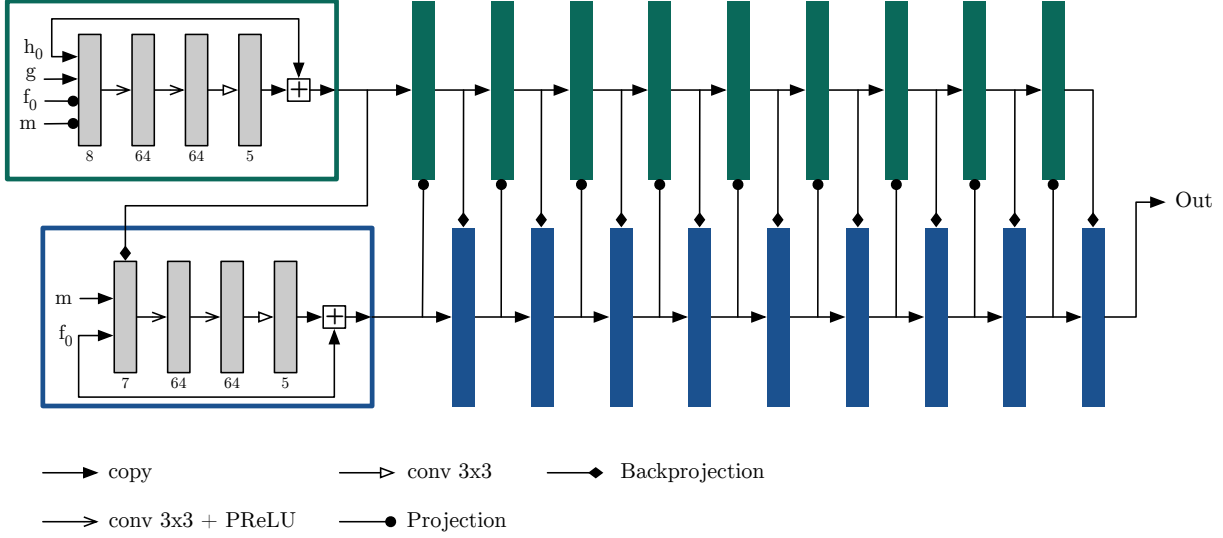


Figure 1: Network architecture of DBToR. Dual blocks (green) are on the upper row and primal blocks (blue) are in the bottom row. The blocks have the same architecture, elaborated in the first blocks. m : the breast thickness mask, h_0 : initial dual vector, f_0 : initial primal vector, g : sinogram data, Out: final reconstruction

header). The algorithm provides a Bayes estimator given by a deep neural network, which is trained to reconstruct the images directly from projection data. The choice of a particular neural network architecture can greatly affect the results and is non-trivial. The DBToR neural network consists of several ‘reconstruction blocks’, which take in projection data, together with information on the thickness of the breast under compression as the initial input, perform a forward and a backward pass by taking projections and back-projections, and use a convolutional neural network to produce an intermediate reconstruction result, which is then improved further by each successive reconstruction block. The architecture of the network is illustrated in Figure 1.

We denote the training set of images $\mathcal{D}_{\text{train}}$. For an image x , we let sinogram_x be the corresponding projection data. We assume that the training data $\mathcal{D}_{\text{train}}$ is a representative sample from the domain of images that we want to reconstruct (DBT images). The neural network is trained in a supervised fashion as follows. We repeatedly sample image $x \sim \mathcal{D}_{\text{train}}$ and the corresponding input projection data $y = \text{sinogram}_x$ from the training dataset. The corresponding thickness mask is denoted by

$m = \text{thickness_mask}_x$ and is represented by a rectangular mask with the same width as the detector and where the height is given by the measured breast thickness after compression. These measurements are provided by the DBT system, and are available both at training and at test time.

Using this information, the reconstruction

$$z := m, y \mapsto \text{compute_reconstruction}(m, y)$$

is given by a deep neural network with parameters θ . We select the L^2 -loss $l_\theta := \|x - z\|_2^2$ to train the network in a supervised fashion. The input projection data is log-transformed, and scaled such that the standard deviation and mean over the training set is 1. The algorithm is described in Figure 2 and the network architecture in Figure 1. In all experiments we set the number of primal blocks N_{prim} and dual blocks N_{dual} to 10. The parameters θ are updated using the Adam optimizer with a cosine annealing learning rate schedule (Loshchilov and Hutter, 2019), i.e. the learning rate in step t was

$$\eta_t = \frac{\eta_0}{2} \left(1 + \cos\left(\pi \frac{t}{N_{\text{iter}}}\right) \right)$$

```

1: procedure COMPUTE_RECONSTRUCTION( $m, g$ )
2:    $f_0 \leftarrow 0 \in X^{N_{\text{prim}}}$   $\triangleright$  Initialize primal vector
3:    $h_0 \leftarrow 0 \in U^{N_{\text{dual}}}$   $\triangleright$  Initialize dual vector
4:   for  $i \leftarrow 0, N$  do
5:      $h_i \leftarrow \Gamma_{\theta_i^d}(h_{i-1}, \mathcal{P}(f_{i-1}^{(2)}), g, \mathcal{P}(m))$ 
6:      $f_i \leftarrow \Lambda_{\theta_i^p}(f_{i-1}, \mathcal{P}^*(h_i^{(1)}), m)$ 
7:   end for
8:   return  $f_I^{(1)}$ 
9: end procedure
10: for  $j \leftarrow 0, N_{\text{iter}} - 1$  do
11:   if  $j$  is divisible by freq then
12:      $x \sim \mathcal{D}_{\text{train}}$   $\triangleright$  Sample train data
13:      $y \leftarrow \text{sinograms}_x$   $\triangleright$  Sample sinograms
14:      $m \leftarrow \text{thickness\_mask}_x$   $\triangleright$  Create masks
15:   end if
16:    $z \leftarrow \text{compute\_reconstruction}(m, y)$ 
17:    $\text{loss} \leftarrow \|z - x\|_2^2$ 
18:   change parameters  $\theta_i^p, \theta_i^d, i = 1, \dots, N$  to reduce loss
19: end for

```

Figure 2: Pseudocode of the DBToR reconstruction algorithm.

starting at a learning rate η_0 of 10^{-3} . The other Adam parameters were the default choices. N_{iter} is the total number of iterations (as in Algorithm 2). $\Gamma_{\theta_i^d}$ and $\Lambda_{\theta_i^p}$ for $i = 1, \dots, I$ are ResNet-type blocks consisting of three convolutional layers with kernel size 3×3 followed by a max pooling layer and 64, 64 and 5 filters respectively. Finally, the operators \mathcal{P} and \mathcal{P}^* are the forward and backward operators respectively. At test time, the algorithm takes the input projection data sinogram_x and the breast thickness information to compute the reconstruction using the function `compute_reconstruction`.

In total, we trained three versions of the DBToR algorithm: two versions were trained on virtual phantom projections, both without any noise and with varying levels of noise, and one version was pretrained on noisy virtual phantom projections and subsequently finetuned on noisy deformed Breast Computed Tomography (BCT) phantoms. This data is described in full detail in Section 3.1 and Section 3.2 respectively. For comparison, we also trained the basic LPD algorithm in addition to DBToR on noise-free virtual phantom projections. This was achieved by removing the height mask from the algorithm input.

2.3. Reconstructed image classification

The final step of the reconstruction for estimation of breast density and radiation dose involved in image acquisition, is the classification of the reconstructed image into skin, adipose, and fibroglandular tissue voxels. This is required because rather than relying on voxel attenuation values, which can be quite similar for different types of tissue, we need correct tissue labels to compute the breast density and the dose absorbed by the fibroglandular tissue. Given its high contrast, the skin layer was segmented through a fast seeded region-growing algorithm (Adams and Bischof, 1994), which grows the segmented region starting from a subset of seeds (corresponding to the voxels located on the outer edge of the skin layer) by subsequently including voxels whose intensity was higher than or equal to the mean seed intensity value. For fibroglandular tissue classification, we extend our previous work on breast CT classification (Caballo et al., 2018), and in the first step remove the skin temporarily from the image, with the resulting representation undergoing a well-established, automatic thresholding method based on fuzzy c-means clustering (Bezdek, 1981), an algorithm generally adopted in the case of images with low noise content, accompanied by a non-negligible degree of blurring, as is the case for our images. Briefly, voxels are iteratively assigned to a given class (adipose or fibroglandular tissue) in an unsupervised fashion, with the iteration stopping criterion aiming at maximizing the distance between the average voxel values of the two classes. As opposed to traditional cluster analysis, this method allows for a degree of fuzzy overlap between the classes over each iteration, which helps classify the boundary voxels in each subsequent iteration. The fuzzy partition term (Bezdek, 1981) was experimentally tuned to a value of 2.0.

3. Materials and Methods

To train and evaluate the algorithm, we created two datasets of 3D breast phantoms from which we extracted the coronal slices and their corresponding DBT projections. The first dataset consists of virtual 3D breast phantoms generated using a stochastic model, while the second is based on patient dedicated BCT images. DBT projections of these phantoms were simulated using deterministic simulation methods, with the posterior addition

of Poisson noise. The use of virtual phantoms not only provided training data, but also allowed for assessing the accuracy of the density and dose estimates, since ground truth is known.

Each voxel of these phantoms was indexed with a label denoting the corresponding tissue type: skin, adipose tissue, fibroglandular tissue, and Cooper's ligaments. The elemental compositions of these materials were obtained from the work of Hammerstein et al. (1979), except for the composition of Cooper's ligaments, which was assumed to be identical to that of fibroglandular tissue. Linear attenuation coefficients at 20 keV, a typical average energy of the spectra in clinical DBT imaging, were calculated for each material using the software from Boone and Chavez (Boone and Chavez, 1996). The resulting linear attenuation coefficients were 0.512 cm^{-1} for adipose tissue, 0.798 cm^{-1} for fibroglandular tissue (and Cooper's ligaments), and 0.854 cm^{-1} for skin.

This process was done for the virtual phantom dataset and the patient BCT dataset.

3.1. Virtual phantom

We extracted 41499 coronal slices from 50 breast phantoms generated using the method of Lau et al. (2012). This method generates breast phantoms in two steps: first, the breast structure is simulated on a coarse scale by generating large compartments of adipose tissue Zhang et al. (2008); Bakic et al. (2011). Second, finer detail for fibroglandular tissue is added subsequently in the form of power-law noise (Reiser and Nishikawa, 2010). An example of the simulated phantoms is shown in Figure 3. These

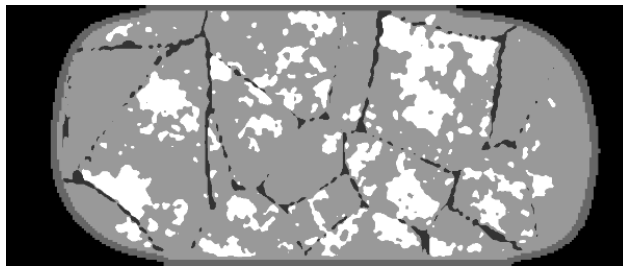


Figure 3: 2D coronal breast phantom containing skin (darkest gray), adipose tissue (dark gray), fibroglandular tissue (light gray), and Cooper's ligaments (black).

41499 coronal slices were used for training and validating

the algorithm. Each breast phantom was either included in a training or validation fold completely or not at all, in order to prevent data contamination and bias.

3.2. Patient dedicated breast CT phantoms

Patient dedicated breast CT images were acquired for an unrelated, ethical-board approved patient study evaluating this imaging technology. The images were released for other research purposes after anonymization. In order to compute the density and the accumulated dose to the fibroglandular tissue, the patient breast CT images were automatically classified into four categories (air, skin, adipose and fibroglandular tissue) using a previously developed algorithm for BCT image classification (Caballo et al., 2018) (see Section 2.3). The classified breasts then underwent simulated mechanical deformation as previously described (Fedon et al., 2019; García et al., 2020). Briefly, the breasts were converted into a finite element (FE) biomechanical model using the package iso2mesh (v.1.8; Matlab v.13a). A large number of 4-node tetrahedral elements, between 100k and 500k, were used in order to minimize the numerical error during the FE analysis (del Palomar et al., 2008). Nearly incompressible (Poisson ratio equal to 0.495), homogeneous and isotropic Neo-Hookean material models for each tissue were used to describe their mechanical behaviour. The Young's modulus for fibroglandular, adipose and skin tissue were set to 4.46 kPa, 15.10 kPa, and 60.00 kPa, respectively (Wellman, 1999). The mechanical compression was then simulated using the open-source package NiftySim (v.2.3.1; University College London) (Johnsen et al., 2015), which uses a Total Explicit Dynamic Lagrangian approach to solve the mechanical FE problem (Miller et al., 2007).

Each breast model was compressed to the thickness recorded in the corresponding DICOM header of the cranio-caudal DBT view of that breast, which was acquired, for clinical purposes, during the same visit as the acquisition of the BCT image.

The total phantom population includes compressed breast thicknesses from 3.0 cm to 5.6 cm and chest wall-to-nipple distances from 5.8 cm to 18.0 cm with an isotropic voxel size of $0.2 \text{ mm} \times 0.2 \text{ mm} \times 0.2 \text{ mm}$, which is more than sufficient for dosimetric applications (Fedon et al., 2019).

Using this method, of which an example is given in Figure 4, we obtained a total of 28891 deformed BCT

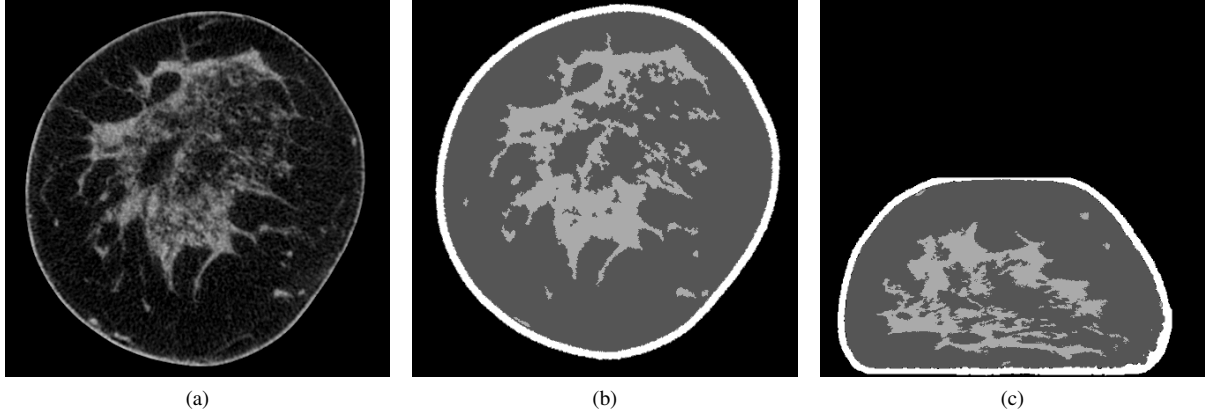


Figure 4: (a) Coronal slice of a breast CT image, (b) the same image classified into skin (white), adipose (dark gray) and fibroglandular (light gray) tissue voxels, and (c) the classified deformed image with the technique described in Section 3.2.

slices extracted from 91 different patient breasts. Given that the number of deformed BCT slices was substantially lower than that of virtual phantom slices, we pre-trained the model with the latter, and then fine-tuned the model using the BCT slices from 46 patient BCT images. The other 45 patient BCT image phantoms were used for testing the reconstruction performance of the model and the accuracy of density and dosimetry estimates. Each patient breast was either completely included or excluded when selecting slices for fine-tuning and testing the model in order to prevent data contamination and bias.

3.3. Projection data

Limited angle fan-beam projections were simulated for all coronal phantom slices using a geometry with the center of rotation placed at the center of the phantom as seen in Figure 5. The x-ray source was placed 65 cm above the center of rotation, and the source-detector distance was 70 cm. A total of 25 equally spaced projections between -24° and 24° were generated, with the detector rotating with the x-ray source. The detector was a perfect photon counting system (100% efficiency) consisting of 1280 elements with a resolution of 0.2 mm.

The forward model

$$\hat{y}_i(\mathbf{x}) = b_i \exp\left(-\sum_j l_{ij} x_j\right)$$

was used for the simulations, with \hat{y} being the simulated projection data, b_i the number of x-ray photons emitted towards detector pixel i , l_{ij} the length of the intersection between voxel j and the line between the source and detector pixel i . The linear attenuation in voxel j is denoted by x_j . For the virtual phantom data, we generated a series of data sets at 3 noise levels from the noiseless simulated projections. This was accomplished by setting photon count $b_i = 1000 \cdot \sqrt{2^N}$ with $N = \{4, 8, 12\}$. For each noise level, a single Poisson noise realization was generated. For the deformed BCT phantoms, only photon counts corresponding to $N = 8$ were used.

Baseline reconstructions were generated for both noiseless and noisy data using 100 iterations of the Maximum Likelihood for Transmission (MLTR) algorithm (Nuyts et al., 1998), using the compressed breast thickness to set the size of the reconstruction volume and with no additional regularization. The MLTR algorithm with smoothing prior and resolution model is competitive with state-of-the-art DBT reconstruction methods (Michielsen, 2016, pp. 165-181). Resolution effects were not included in the computation and thus were not needed in the reconstruction. The smoothing prior was not included because it does not influence the spatial distribution of fibroglandular tissue in the reconstruction.

3.4. Density computation

Breast density by mass, also called glandularity (G), was computed as follows:

$$G = \frac{N_g \rho_g}{N_g \rho_g + N_a \rho_a} \quad (5)$$

where N_g is the number of voxels classified as fibroglandular tissue, N_a is the number of voxels classified as adipose tissue, and ρ_g and ρ_a are the corresponding density for fibroglandular and adipose tissue, respectively, according to Hammerstein et al. Hammerstein et al. (1979). The true breast density of each BCT phantom was obtained by applying this equation to the phantom volumes themselves. The estimated breast density resulting from the proposed method was obtained by applying the equation to the classified reconstructed images.

3.5. Dose calculation

The mean glandular dose (MGD) estimations were performed using a previously described and validated Monte Carlo code (Fedon et al., 2018a,b), based on the Geant4 toolkit (release 10.05, December 2018). The Monte Carlo geometry replicates the one used to generate the projections and is shown in Figure 5.

As during simulation of the DBT projections above, each voxel was labelled with an index related to its composition: air, adipose tissue, fibroglandular tissue, and skin, using the chemical compositions reported by Hammerstein et. al. Hammerstein et al. (1979).

The energy deposited in the fibroglandular voxels was recorded and then converted into dose according to the formula

$$\text{MGD} = \frac{\sum_i E_i}{M_g} \quad (6)$$

where E_i is the energy deposited at the interaction event i , and M_g is the total fibroglandular breast mass.

10^7 primary x-rays were emitted by an isotropic point source placed at 70 cm from the detector and collimated to irradiate the entire detector. In order to replicate the tomosynthesis acquisition mode, a total of 25 projections were simulated from -24° to 24° , every 2° . The projection at 0° replicates the mammographic acquisition. The number of primary particles ensured a statistical uncertainty on the total dose of less than 0.7%, evaluated using

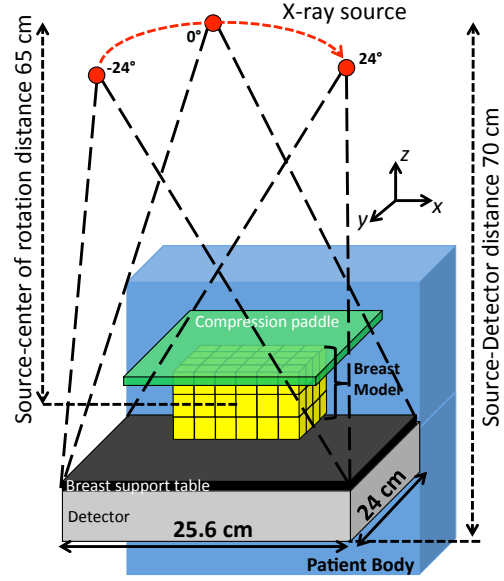


Figure 5: Imaging geometry implemented in the Monte Carlo simulation: the x-ray source is placed at 70 cm from the detector, a 3 mm thick polyethylene terephthalate (PET) compression paddle was simulated and a large water cuboid was included to take into account the patient-body backscatter. The x-ray field irradiated the breast model at different angles (from -24° to 24°). The center of rotation is placed at 65 cm from the x-ray source. Drawing is not to scale and rotation of the detector is not shown.

Table 1: X-ray spectra used in the Monte Carlo simulation. HVL: 1st half value layer

Breast Thickness (mm)	Spectrum	HVL (mm Al)	# Cases
30-39	W/Rh - 27 kV	0.519	2
40-49	W/Rh - 28 kV	0.530	7
50-59	W/Rh - 29 kV	0.538	6
60-69	W/Rh - 30 kV	0.547	18
70-79	W/Rh - 31 kV	0.557	12

the method proposed by Sempau et al. (2001). Photoelectric interactions, and coherent and incoherent scatter were included in the simulations without modifying the default cut range for photons (1 mm, corresponding to an energy of 2.45 keV and 2.88 keV for adipose and fibroglandular tissue, respectively).

The x-ray spectra were modeled using the TASMICS

model (Hernandez and Boone, 2014) by adjusting the thickness of the modeled rhodium filter to match the first half-value layer measured with a solid state detector (RaySafe X2-MAM sensor, Billdal, Sweden) in the modelled system as shown in Table 1. The Monte Carlo simulations for estimating the MGD were performed twice for each breast; once for each of the 45 BCT phantoms, and once each for the corresponding labelled DBToR reconstructions. In this way, the accuracy of the resulting patient-specific dosimetry estimates could be assessed.

3.6. Comparison to current reconstructions

The results of the DBToR reconstruction, prior to the voxel classification for estimation of breast density and dose, were compared to the baseline iterative MLTR reconstruction algorithm and the LPD algorithm. The LPD algorithm was trained using the noiseless version of the simulated projections.

4. Results

All models were trained on a single NVidia Titan X GPU with 12 GB of memory and batch size 1, the number of iterations N_{iter} was set to $4 \cdot 10^5$ for all models. Training each model took approximately a week. At inference stage, the reconstruction takes around 1 second for a single coronal slice. For DBToR trained on noise-free virtual phantom data we report the corresponding L^2 loss, Structural Similarity Index (SSIM) (Wang et al., 2004) and Peak Signal-to-Noise Ratio (PSNR) on noise-free virtual phantom test data in Table 2. Lower L^2 loss and higher SSIM and PSNR values indicate better reconstruction performance. For DBToR trained on noisy virtual phantom projections, where we used noise level $N = 8$ only during training, we report these metrics for noise levels $N = 4, 8, 12$ in Table 3. In both tables, we report the mean and standard deviation of the metrics obtained using 3 cross-validation folds with 50% of the data used for training and 50% used for testing in each fold.

The LPD algorithm is significantly outperformed in the noise-free case. Visual inspection of the slices produced by LPD revealed that the LPD often reconstructs breast regions adjacent to the compression paddle very poorly for both test and training data. In particular, it frequently fails to reproduce the flatness of the part of the skin surface

which is in contact with the compression paddle. Since the same type of reconstruction artifacts appear for both training and test data, we ruled out overfitting of LPD as the cause of the artifacts. While it is possible that a much larger version of LPD with more reconstruction blocks would learn to correct these artifacts, we will see that DBToR resolves them without any further increase in the number of parameters. Since LPD performed poorly on noise-free projections (see Table 2), we excluded it from further training on noisy projections. The proposed DBToR algorithm outperforms the MLTR reconstruction algorithm at all noise levels and for all metrics being considered, while yielding visually more accurate reconstructions as well. It is also interesting to note from Table 3 that the performance of DBToR at noise level $N = 4$ is comparable to the MLTR reconstruction algorithm at noise level $N = 8$, which corresponds to a 4 times higher photon count. At noise level $N = 12$, the performance of MLTR is slightly below the performance of MLTR for the noise-free case. At the same time, DBToR at $N = 12$ reaches comparable level of performance to that of the DBToR on noise-free data, which can be seen from slightly higher PSNR and slightly lower SSIM as compared to the noise-free version.

For DBToR trained on noisy virtual phantom projections and subsequently finetuned on deformed breast CT slices, where we used noise level $N = 8$ only during training and finetuning, we summarize the reconstruction performance in Table 4, and in Figures 9, 10, and 11 we give examples of coronal, axial, and sagittal slices of the virtual breast phantom and corresponding MLTR reconstruction, DBToR reconstruction, and DBToR classification (all on noisy deformed breast CT slices). We observe that DBToR outperforms the baseline MLTR algorithm in terms of the reported metrics and visual quality of the slices, particularly noticeable for coronal and sagittal directions.

4.1. Breast density estimation

Figure 6 shows a box-whisker plot of the absolute percentage difference in glandularity between the DBToR estimate and the ground truth (GT). It can be seen that, on average, no bias is observed (p -value 0.3), and that the breast density estimates are accurate to within 2%, and almost always within two standard deviations of the mean.

Table 2: Results on noise-free phantom projections, mean \pm standard deviation (in bold best result)

Model	L^2 -loss	SSIM	PSNR
MLTR	$0.00773 \pm 4.3 \cdot 10^{-5}$	$0.83 \pm 4.2 \cdot 10^{-3}$	$20.19 \pm 2.9 \cdot 10^{-2}$
LPD	$0.038 \pm 3.8 \cdot 10^{-2}$	$0.38 \pm 1.8 \cdot 10^{-1}$	16.1 ± 5.7
DBToR	$0.0024 \pm 3.0 \cdot 10^{-4}$	$0.89 \pm 1.0 \cdot 10^{-2}$	$25.8 \pm 5.5 \cdot 10^{-1}$

Table 3: Results on noisy phantom projections for different noise levels N , mean \pm standard deviation (in bold best result)

Model	L^2 -loss	SSIM	PSNR
MLTR ($N = 4$)	$0.0096 \pm 1.0 \cdot 10^{-4}$	$0.6788 \pm 9 \cdot 10^{-3}$	$19.17 \pm 5.8 \cdot 10^{-2}$
DBToR ($N = 4$)	$0.0075 \pm 2.3 \cdot 10^{-3}$	$0.7528 \pm 6.4 \cdot 10^{-2}$	20.78 ± 1.18
MLTR ($N = 8$)	$0.0082 \pm 5.2 \cdot 10^{-5}$	$0.7463 \pm 7.2 \cdot 10^{-3}$	$19.87 \pm 3.6 \cdot 10^{-2}$
DBToR ($N = 8$)	$0.0021 \pm 9.7 \cdot 10^{-5}$	$0.8612 \pm 6.0 \cdot 10^{-2}$	$26.54 \pm 2.5 \cdot 10^{-1}$
MLTR ($N = 12$)	$0.0078 \pm 4.47 \cdot 10^{-5}$	$0.7977 \pm 5.5 \cdot 10^{-3}$	$20.06 \pm 3.0 \cdot 10^{-2}$
DBToR ($N = 12$)	$0.0019 \pm 1.3 \cdot 10^{-4}$	$0.8689 \pm 6.2 \cdot 10^{-2}$	$26.62 \pm 2.8 \cdot 10^{-1}$

Table 4: Results on noisy BCT phantom projections (in bold best result)

Model	L^2 -loss	SSIM	PSNR
MLTR	0.006	0.82	21.45
DBToR	0.0018	0.93	27.03

4.2. Mean glandular dose estimation

The comparison between the MGD evaluated from the DBToR reconstructions and the GT is shown in the Bland-Altman plots of Figure 7, for both mammography and DBT geometries.

As can be seen, no bias is observed in the proposed dose estimation method (p -value 0.23), with the data points equally scattered around zero, and that the largest error in the dose estimation is less than 20%. Visual inspection of the cases that lie beyond the limits reveals that this is the consequence of differences in the reconstructed fibroglandular distribution obtained with the DBToR model compared to the GT, as shown in an example in Figure 8.

For this case, the absolute difference on the glandularity is 1.5% (namely 12.0% for the DBToR and 13.5% for GT). Thus, due to a higher amount of fibroglandular tissue closest to the x-ray source in the case of the GT, the radiation dose estimated by DBToR is lower by 13.5%.

5. Discussion and conclusion

We presented a deep learning-based method for the reconstruction of DBT, which we call DBToR. The model is both data driven and model-based, since the forward and backprojection operators for a given DBT geometry are a part of our neural network architecture and at the same time the model is trained to reduce the tomographic artifacts of the reconstruction. As training data we used two sources of data, one based on random samples with statistical properties similar to real breast volumes, and one dataset of patient breast CT images that have been compressed with a finite element model to simulate the same breast under compression in a DBT system.

Compared to LPD, in DBToR we added the compressed breast thickness as prior information. Since the limited angle causes a severely ill-posed problem, it was expected that this information would be definitely required, and the experiments (Table 2) confirmed that the result dramatically degrades, compared to the 'full' DBToR, when this prior knowledge is not provided to the algorithm. Requiring this additional information does not limit the generalizability of the method, since it is readily available in all DBT systems.

The results indicate that the proposed algorithm outperforms the MLTR iterative reconstruction in terms of re-

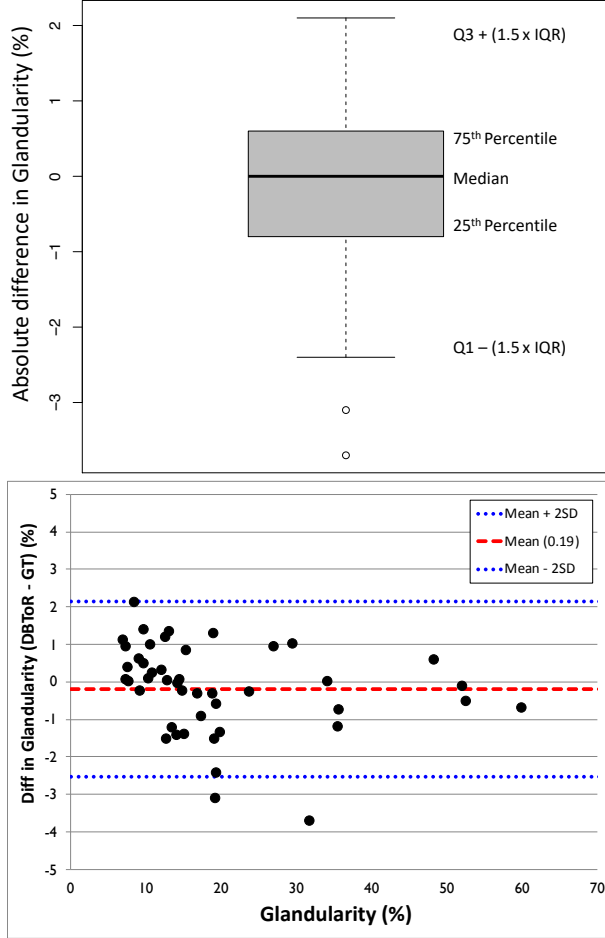


Figure 6: (top) Box-whisker plot and (bottom) Bland-Altman plot of the absolute difference (DBToR - GT) of glandularity (in percentage). The symbols in the box-whisker plot denote outliers.

construction quality for this application. Furthermore, the algorithm generalizes well even when trained on a small dataset and is robust to noise.

The simulated acquisitions in this work used a mono-energetic beam and did not include x-ray scattered radiation, so it remains to be seen how our new reconstruction method will handle these factors. In practice the effect of not modeling the spectrum will likely be minimal as regular filtered backprojection reconstructions also do not account for these physical effects and apply a series of pre-correction steps to the projection data instead, such as the beam hardening correction described by Herman (1979). We foresee using the same approach to extend our method to work in clinical data.

We have shown that the method achieves robust and accurate predictions of breast density, which is an important metric relating to masking and cancer risk. As opposed to current density estimation methods based on mammography and DBT projections, which require assumptions and modeling of the image acquisition process, the use of the images produced by DBToR allows for a direct estimation of the amount of dense tissue present in the volume, resulting in estimates to within 3%. Accurate determination of breast density opens up further opportunities for personalized risk-based screening. As is crucial for an accurate dosimetric estimate, the location in the vertical direction of the dense tissue is also estimated with accuracy, resulting in a state-of-the-art dosimetric estimate. It is known that current model dose estimates introduce an average bias of 30%, and can misrepresent the actual patient-specific dose by up to 120% (Dance et al., 2005; Sechopoulos et al., 2012; Hernandez et al., 2015). In comparison, the results obtained here achieve errors below 20% with no systematic bias. True patient-specific dosimetry could be used, for the first time, to gather dose registries, especially for screening, ensuring the optimal use of this imaging technology, and allowing for continuous monitoring of dose trends and providing valuable data for additional optimization and development of existing and new imaging technologies.

The main limitation of the current work is that it works on a slice by slice basis rather than on a full 3D volume. With this simplification we were able to concentrate on the network structure rather than on the logistics of handling the enormous datasets needed to train a 3D model.

The logical next step for our algorithm is an extension

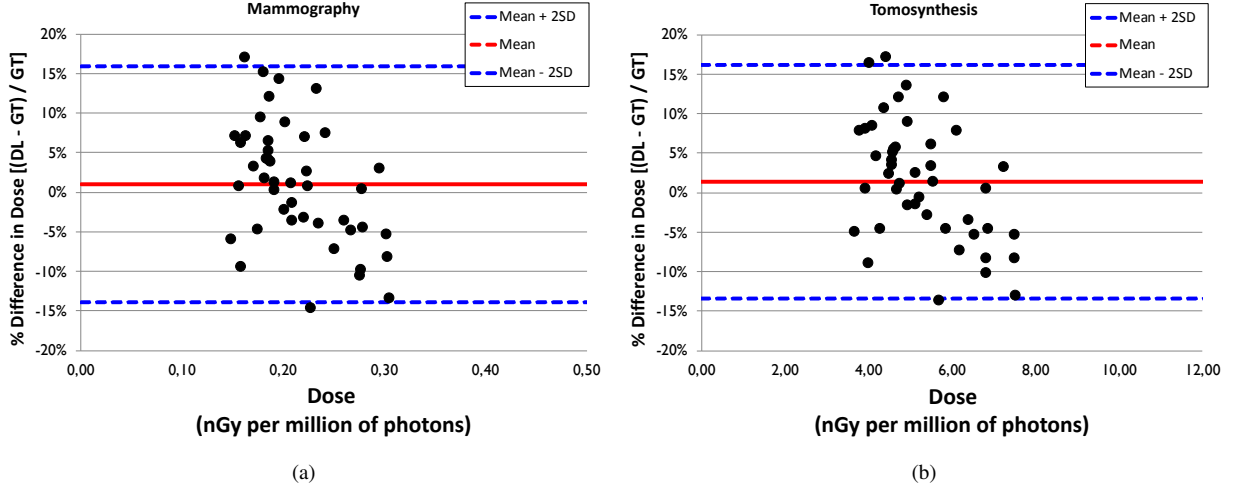


Figure 7: Bland-Altman plot of the difference in dose estimates resulting from the DBToR reconstruction and the ground truth, in percentage, for both mammography (a) and DBT (b). The red line represents the mean, while the two blue-dashed lines represent the 95% limits of agreement.

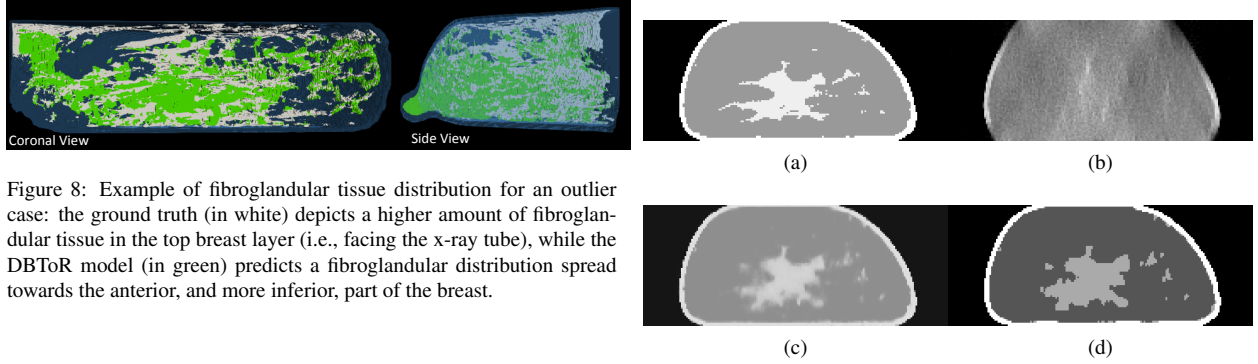


Figure 8: Example of fibroglandular tissue distribution for an outlier case: the ground truth (in white) depicts a higher amount of fibroglandular tissue in the top breast layer (i.e., facing the x-ray tube), while the DBToR model (in green) predicts a fibroglandular distribution spread towards the anterior, and more inferior, part of the breast.

to fully 3D data instead of 2D slices. From there on, we could extend the model-based parts of the deep learning network instead of starting from precorrected projection data, as in current filtered backprojection methods, by including a polychromatic x-ray spectrum, x-ray scatter, and other relevant factors in the forward model. It could also be valuable to optimize the network output specifically for artificial intelligence reading by training the composite network in an end-to-end fashion. Finally, the reconstruction of a diagnostic-quality volume, for interpretation by radiologists, with the potential for the higher vertical resolution obtained here, would be a valuable improvement for clinical performance.

To conclude, we created a deep learning based recon-

Figure 9: (a) Coronal slice of a breast CT phantom, (b) MLTR reconstruction, (c) DBToR reconstruction, and (d) classification of DBToR reconstruction.

struction for DBT that was able to achieve accurate predictions of breast density and from there an accurate calculation of patient specific MGD.

Acknowledgments

The research was partially supported by National Cancer Institute, National Institutes of Health:

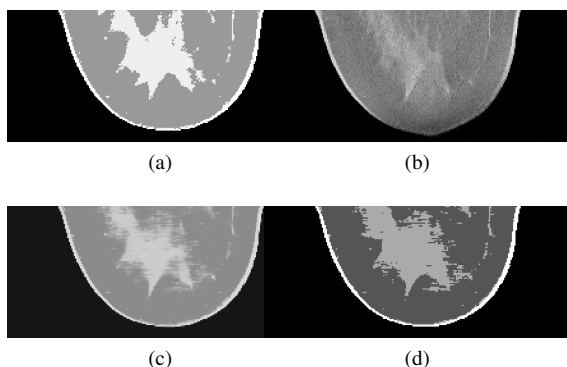


Figure 10: (a) Axial slice of a breast CT phantom, (b) MLTR reconstruction, (c) DBToR reconstruction, and (d) classification of DBToR reconstruction.

7R01CA181171 Susan G. Komen Foundation for the Cure: IIR13262248.

References

- Adams, R., Bischof, L., 1994. Seeded Region Growing. *IEEE Transactions on Pattern Analysis and Machine Intelligence* 16.
- Adler, J., Öktem, O., 2018. Learned Primal-Dual Reconstruction. *IEEE Transactions on Medical Imaging* 37, 1322–1332. doi:10.1109/TMI.2018.2799231.
- Arana Peña, L.M., Fedon, C., Garcia, E., Diaz, O., Longo, R., Dance, D.R., Sechopoulos, I., 2020. Monte Carlo dose evaluation of different fibroglandular tissue distribution in breast imaging, in: Van Ongeval, C., Marshall, N., Bosmans, H. (Eds.), 15th International Workshop on Breast Imaging (IWBI2020), SPIE. p. 76. doi:10.1117/12.2564278.
- Arridge, S., Maass, P., Öktem, O., Schönlieb, C.B., 2019. Solving inverse problems using data-driven models. *Acta Numerica* 28, 1174. doi:10.1017/S0962492919000059.
- Bakic, P.R., Zhang, C., Maidment, A.D.A., 2011. Development and characterization of an anthropomorphic breast software phantom based upon region-growing algorithm. *Medical Physics* 38, 3165–3176. URL: <http://doi.wiley.com/10.1118/1.3590357>, doi:10.1118/1.3590357.
- Bezdek, J.C., 1981. Pattern recognition with fuzzy objective function algorithms. Plenum, New York, NY.
- Boone, J.M., Chavez, A.E., 1996. Comparison of x-ray cross sections for diagnostic and therapeutic medical physics. *Medical Physics* 23, 1997–2005. URL: <http://doi.wiley.com/10.1118/1.597899>, doi:10.1118/1.597899.
- Caballo, M., Boone, J., Mann, R., Sechopoulos, I., 2018. An unsupervised automatic segmentation algorithm for breast tissue classification of dedicated breast computed tomography images. *Medical Physics* 45, 2542–2559.
- Dance, D.R., Sechopoulos, I., 2016. Dosimetry in x-ray-based breast imaging. *Physics in Medicine and Biology* 61, R271–R304. doi:10.1088/0031-9155/61/19/R271.
- Dance, D.R., et al., 2005. Breast dosimetry using high-resolution voxel phantoms. *Radiation Protection Dosimetry* 114, 359–363. doi:10.1093/rpd/nch510.
- Fedon, C., Caballo, M., Longo, R., Trianni, A., Sechopoulos, I., 2018a. Internal breast dosimetry in mammography: Experimental methods and Monte Carlo validation with a monoenergetic x-ray beam. *Medical Physics* 45, 1724–1737. doi:10.1002/mp.12792.
- Fedon, C., Caballo, M., Sechopoulos, I., 2018b. Internal breast dosimetry in mammography: Monte Carlo validation in homogeneous and anthropomorphic breast phantom with a clinical mammography system. *Medical Physics* 45, 3950–3961. doi:10.1002/mp.13069.
- Fedon, C., et al., 2019. Monte Carlo study on optimal breast voxel resolution for dosimetry estimates in digital breast tomosynthesis. *Physics in Medicine & Biology* 64, 015003. doi:10.1088/1361-6560/aaf453.
- Förnvik, D., Timberg, P., Zackrisson, S., Tingberg, A., Petersson, H., Dustler, M., 2018. Towards determination of individual glandular dose, in: Chen, G.H., Lo, J.Y., Gilat Schmidt, T. (Eds.), *Medical Imaging 2018: Physics of Medical Imaging*, SPIE. p. 3. doi:10.1117/12.2293454.

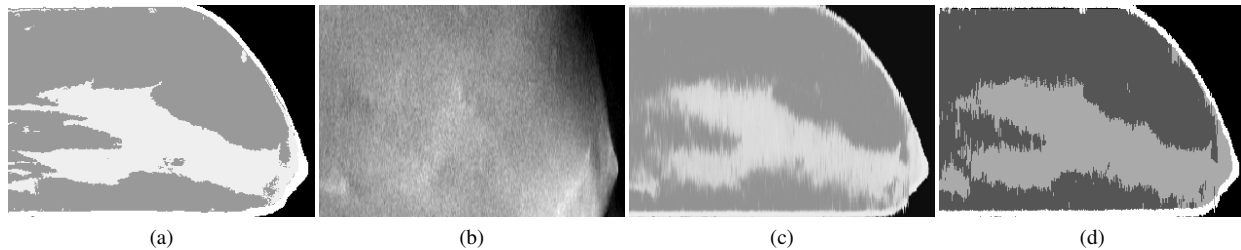


Figure 11: (a) Sagittal slice of a breast CT phantom, (b) MLTR reconstruction, (c) DBToR reconstruction, and (d) classification of DBToR reconstruction.

- García, E., Fedon, C., Caballo, M., Martí, R., Sechopoulos, I., Diaz, O., 2020. Realistic compressed breast phantoms for medical physics applications, in: Van Ongeval, C., Marshall, N., Bosmans, H. (Eds.), 15th International Workshop on Breast Imaging (IWBI2020), SPIE. p. 73. doi:10.1117/12.2564273.
- Geeraert, N., 2014. Quantitative evaluation of fibroglandular tissue for estimation of tissue-differentiated absorbed energy in breast tomosynthesis. Ph.D. thesis. KU Leuven. Faculty of medicine.
- Hammerstein, R., Miller, D.W., White, D.R., Masterson, E., Woodard, H.Q., Laughlin, J.S., 1979. Absorbed Radiation Dose in Mammography. *Radiology* 130, 485–491. URL: <http://pubs.rsna.org/doi/10.1148/130.2.485>, doi:10.1148/130.2.485.
- Herman, G.T., 1979. Correction for beam hardening in computed tomography. *Physics in Medicine and Biology* 24, 008. URL: <https://iopscience.iop.org/article/10.1088/0031-9155/24/1/008>, doi:10.1088/0031-9155/24/1/008.
- Hernandez, A., Boone, J., 2014. Tungsten anode spectral model using interpolating cubic splines: unfiltered x-ray spectra from 20 kV to 640 kV. *Medical Physics* 41, 042101.
- Hernandez, A.M., Seibert, J.A., Boone, J.M., 2015. Breast dose in mammography is about 30% lower when realistic heterogeneous glandular distributions are considered. *Medical Physics* 42, 6337–6348. doi:10.1118/1.4931966.
- Johnsen, S.F., et al., 2015. NiftySim: A GPU-based non-linear finite element package for simulation of soft tissue biomechanics. *Int J Comput Assist Radiol Surg* 10, 1077–1095. doi:10.1007/s11548-014-1118-5.
- Lau, B.A., Reiser, I., Nishikawa, R.M., Bakic, P.R., 2012. A statistically defined anthropomorphic software breast phantom. *Medical Physics* 39, 3375–3385. URL: <http://doi.wiley.com/10.1118/1.4718576>, doi:10.1118/1.4718576.
- Loshchilov, I., Hutter, F., 2019. SGDR: Stochastic gradient descent with warm restarts, in: 5th International Conference on Learning Representations, ICLR 2017 - Conference Track Proceedings, pp. 1–16.
- McCormack, V.A., 2006. Breast Density and Parenchymal Patterns as Markers of Breast Cancer Risk: A Meta-analysis. *Cancer Epidemiology Biomarkers & Prevention* 15, 1159–1169. URL: <http://cebp.aacrjournals.org/cgi/doi/10.1158/1055-9965.EPI-06-0034>, doi:10.1158/1055-9965.EPI-06-0034.
- Michielsen, K., 2016. Maximum a posteriori reconstruction for digital breast tomosynthesis. Ph.D. thesis. KU Leuven. Faculty of medicine. Leuven.
- Michielsen, K., Nuyts, J., Cockmartin, L., Marshall, N., Bosmans, H., 2016. Design of a model observer to evaluate calcification detectability in breast tomosynthesis and application to smoothing prior optimization. *Medical Physics* 43, 6577–6587. doi:10.1118/1.4967268.
- Miller, K., Joldes, G., Lance, D., Wittek, A., 2007. Total Lagrangian explicit dynamics finite element algorithm

- for computing soft tissue deformation. *Communications in Numerical Methods in Engineering* 23, 121–134. doi:10.1002/cnm.887.
- Moriakov, N., Michielsen, K., Adler, J., Mann, R., Sechopoulos, I., Teuwen, J., 2019. Deep learning framework for digital breast tomosynthesis reconstruction, in: Bosmans, H., Chen, G.H., Gilat Schmidt, T. (Eds.), *Medical Imaging 2019: Physics of Medical Imaging*, SPIE. p. 220. doi:10.1117/12.2512912.
- Niklason, L.T., et al., 1997. Digital tomosynthesis in breast imaging. *Radiology* 205, 399–406. doi:10.1148/radiology.205.2.9356620.
- Nuyts, J., Man, B.D., Dupont, P., Defrise, M., Suetens, P., Mortelmans, L., 1998. Iterative reconstruction for helical CT: a simulation study. *Physics in Medicine and Biology* 43, 729–737. doi:10.1088/0031-9155/43/4/003.
- del Palomar, A.P., Calvo, B., Herrero, J., Lopez, J., Doblare, M., 2008. A finite element model to accurately predict real deformations of the breast. *Med Eng Phys* 30, 1089–1097. doi:10.1016/j.medengphy.2008.01.005.
- Plevritis, S.K., et al., 2018. Association of screening and treatment with breast cancer mortality by molecular subtype in US women, 2000–2012. *JAMA - Journal of the American Medical Association* 319, 154–164. doi:10.1001/jama.2017.19130.
- Reiser, I., Nishikawa, R.M., 2010. Task-based assessment of breast tomosynthesis: Effect of acquisition parameters and quantum noise. *Medical Physics* 37, 1591–1600. URL: <http://doi.wiley.com/10.1118/1.3357288>, doi:10.1118/1.3357288.
- Rodriguez-Ruiz, A., et al., 2017. New reconstruction algorithm for digital breast tomosynthesis: better image quality for humans and computers. *Acta Radiologica*.
- Sechopoulos, I., Bliznakova, K., Qin, X., Fei, B., Feng, S.S.J., 2012. Characterization of the homogeneous tissue mixture approximation in breast imaging dosimetry. *Medical Physics* 39, 5050–5059. doi:10.1118/1.4737025.
- Sempau, J., Sanchez-Reyes, A., Salvat, F., Tahar, H., Jiang, S., Fernandez-Varea, J., 2001. Monte Carlo simulation of electron beams from an accelerator head using PENELOPE. *Physics in Medicine and Biology* 46, 1163–1186.
- Wang, Z., Bovik, A., Sheikh, H., Simoncelli, E., 2004. Image Quality Assessment: From Error Visibility to Structural Similarity. *IEEE Transactions on Image Processing* 13, 600–612. URL: <http://ieeexplore.ieee.org/document/1284395/>, doi:10.1109/TIP.2003.819861.
- Wellman, P.S., 1999. Tactile imaging. Ph.D. thesis. Harvard University.
- Zackrisson, S., et al., 2018. One-view breast tomosynthesis versus two-view mammography in the malm breast tomosynthesis screening trial (mbtst): a prospective, population-based, diagnostic accuracy study. *The Lancet Oncology* 19, 1493–1503.
- Zhang, C., Bakic, P.R., Maidment, A.D.A., 2008. Development of an anthropomorphic breast software phantom based on region growing algorithm, in: Miga, M.I., Cleary, K.R. (Eds.), *Medical Imaging 2008: Visualization, Image-Guided Procedures, and Modeling*, p. 69180V. doi:10.1117/12.773011.
- Zuley, M.L., et al., 2013. Digital breast tomosynthesis versus supplemental diagnostic mammographic views for evaluation of noncalcified breast lesions. *Radiology* 266, 89–95. doi:10.1148/radiol.12120552.